

See discussions, stats, and author profiles for this publication at: <https://www.researchgate.net/publication/257573493>

# The influence of surface coverage on textural, structural and catalytic properties of cesium salts of 12-molybdophosphoric acid supported on SBA-15 mesoporous silica. Micropor. Mes...

**ARTICLE** in MICROPOROUS AND MESOPOROUS MATERIALS · SEPTEMBER 2012

Impact Factor: 3.45 · DOI: 10.1016/j.micromeso.2012.02.030

---

CITATIONS

16

---

READS

109

## 3 AUTHORS:



**Alexandru Popa**

Institute of Chemistry Timisoara, Romania

96 PUBLICATIONS 272 CITATIONS

SEE PROFILE



**Viorel Zoltan Sasca**

Institute of Chemistry Timisoara-Romanian...

62 PUBLICATIONS 224 CITATIONS

SEE PROFILE



**Ivanka Holclajtner-Antunović**

University of Belgrade

99 PUBLICATIONS 428 CITATIONS

SEE PROFILE



# The influence of surface coverage on textural, structural and catalytic properties of cesium salts of 12-molybdophosphoric acid supported on SBA-15 mesoporous silica

Alexandru Popa<sup>a,\*</sup>, Viorel Sasca<sup>a</sup>, Ivanka Holclajtner-Antunović<sup>b</sup>

<sup>a</sup> Institute of Chemistry Timișoara, B1. Mihai Viteazul 24, 300223 Timișoara, Romania

<sup>b</sup> Faculty of Physical Chemistry, University of Belgrade, P.O. Box 47, 11158 Belgrade, Serbia

## ARTICLE INFO

### Article history:

Received 18 June 2011

Received in revised form 31 January 2012

Accepted 18 February 2012

Available online 28 February 2012

### Keywords:

Heteropolyacids

Cs salts of molybdophosphoric acid

SBA 15

Characterization

Ethanol conversion

## ABSTRACT

The Cs salt of molybdophosphoric acid  $\text{Cs}_{2.5}\text{H}_{0.5}\text{PMo}_{12}\text{O}_{40}$  (CsHPM) was supported on SBA-15 in the concentration of 20, 30 and 40 wt.% loadings. Because Cs acid salts are insoluble, the SBA-15 supported Cs-acid salts were prepared by two-step sequential impregnation and in situ reaction on the support. The structure and texture of these CsHPM/SBA-15 composites were studied by XRD, SEM-EDS, FT-IR and micro-Raman spectroscopy and  $\text{N}_2$  adsorption. Thermal stability was investigated by thermogravimetric analysis (TGA), differential thermal analysis (DTA) and differential scanning calorimetry (DSC). The dehydration of ethanol was used to probe the catalytic properties of the CsHPM samples incorporated on the silica matrix. FT-IR and Raman studies demonstrated that CsHPM maintained its Keggin structure after deposition on mesoporous SBA-15, regardless of the active phase concentration. The values of specific surface area of pure CsHPM were increased by deposition on mesoporous silica support. The immobilization of CsHPM on mesoporous SBA-15 obviously increases the thermal stability of the Keggin structures in comparison with their parent bulk Cs salts. The main reaction products obtained on acid (dehydration) catalytic centres were ethylene and diethyl ether, and respectively acetaldehyde which was obtained on redox (dehydrogenation) catalytic centres.

© 2012 Elsevier Inc. All rights reserved.

## 1. Introduction

Heteropolyacids (HPAs) with Keggin structure and their salts unsupported and supported on different materials may be used for both acid and redox catalysis, as well as in media as heterogeneous (gas–solid and liquid–solid systems) or homogeneous catalysts [1–3]. As pure heteropolyacids have some drawbacks of low surface area, relatively low thermal stability and high solubility in water and polar solvents, they are usually impregnated on different porous materials with high surface area (hexagonal mesoporous silica, titania, polymers, molecular sieves) [4–10].

Among these carriers, amorphous silica has been used most frequently as it interacts weakly with the Keggin anions and thus preserves their structure. During the last 10–15 years HPAs supported on mesoporous siliceous materials MCM-41 and SBA-15 have attracted much attention due to its very high surface area coupled with regular hexagonal array of uniform pore sizes within the mesoporous region. SBA-15 is a suitable support for acid catalysts as compared with MCM-41 possesses thicker pore walls, larger pore sizes and higher thermal and hydrothermal stability.

Although HPAs are strong and useful solid acids, the amount of acidic sites on their surface is small because of their low surface area. Therefore, increasing the amount of surface acidic sites is an important task for the development of useful solid acids applied in different catalyzed reactions. Different attempts have been made to improve the efficiency of the HPAs by supporting on various high surface area supports and by replacement of protons with alkali metals [11–18].

In the literature very few references have been reported concerning  $\text{H}_3[\text{PMo}_{12}\text{O}_{40}]$  (HPM) and  $\text{H}_4[\text{PMo}_{11}\text{VO}_{40}]$  supported on mesoporous materials, majority of the studies have been focused on investigation the most acidic HPAs in the series, namely  $\text{H}_3\text{PW}_{12}\text{O}_{40}$  (HPW) [5,19–21,6,22–24].

Liu et al. [5] reported that in the isopropylation of naphthalene with isopropanol, HPW/SBA-15 catalysts exhibit much higher conversions than that of pure HPW, and the conversion of naphthalene increases substantially with the increase of PW loadings. Moreover, the HPW/SBA-15 catalyst is more catalytically active than HPW/MCM-41 and HPW/ $\text{SiO}_2$  catalysts in this reaction. HPW immobilized onto the surface of amine-modified mesoporous sieve SBA-15 were evaluated for the liquid-phase oxidation of cyclopentene with 50% hydrogen peroxide as the oxidant in tert butanol. A 100% conversion of cyclopentene and an 81% selectivity for

\* Corresponding author. Tel.: +40 256 491818; fax: +40 256 491824.

E-mail address: [alpopa\\_tim2003@yahoo.com](mailto:alpopa_tim2003@yahoo.com) (A. Popa).

glutaraldehyde were obtained and these were higher than that for the catalysts prepared by direct impregnation [19]. Sheng et al. [20] reported that 30% HPW/LaSBA-15 catalyst had high strength of acidic sites and good catalytic activity in the alkylation of o-xylene with styrene. Compared with 30% HPW/SBA-15 catalyst, the 30% HPW/LaSBA-15 one had better regeneration, which was due to the strong interaction between the HPW and the support in the presence of La, thus prevent HPW leaching from the support.

Entrapment of HPW by sol–gel technique into the mesoporous molecule sieve SBA-15 increased the hydrothermal stability which was studied by washing the samples with an EtOH/H<sub>2</sub>O mixture and conducting esterification involving polar solvents. The sol–gel derived composite is more stable in the acidic property and the structural regularity of the mesoporous material than the impregnated sample [21].

The effect of nickel salt of 12-tungstophosphoric acid, Ni<sub>3/2</sub>PW<sub>12</sub>O<sub>40</sub>, as oxide precursors and of hetero-atoms modifying SBA-15 on the activity of NiW/(Al-, Ti-, W-)SBA-15 catalysts was reported in thiophene hydrodesulphurization reaction [6]. The NiW catalyst supported on W- containing SBA-15 showed higher performance in the HDS of thiophene as compared to the SBA-15 modified with Al and Ti. A series of Mo (W) catalysts promoted by Ni and supported on SBA-15 was prepared using Keggin-type heteropolyacids (HPM or HPW) as active phase precursors. It was found that both Mo and W catalysts prepared from heteropolyacids showed better performance in hydrodesulphurization of 4,6-dimethyldibenzothiophene than the counterparts prepared from traditionally used Mo (W) ammonium salts [22].

Tungstophosphoric acid (HPW), molybdophosphoric acid (HPM) and tungstosilicic acid (HSiW) immobilized on SBA-15 were used, as catalysts, in the esterification of palmitic acid with methanol. It was observed that the catalytic activity decreases in the following series: HPW-SBA-15 > HSiW-SBA-15 > HPM-SBA-15 [23]. HPM was successfully encapsulated into the super cage of Y zeolite promoted by Cs counter cation in zeolite matrix, using 2.5% aqueous solution of Cs<sub>2</sub>CO<sub>3</sub>. The 30% HPM-CsY catalyst exhibits considerable catalytic activity in liquid phase esterification of acetic acid with n-butanol under the optimal reaction conditions [24].

By substitution of H<sup>+</sup> protons with alkaline cations, important modifications take place on the surface area, pore structure, solubility and hydrophobicity, in comparison to the parent HPA. HPAs salts with large monovalent ions, such as NH<sub>4</sub><sup>+</sup>, K<sup>+</sup>, Rb<sup>+</sup>, Cs<sup>+</sup>, Ag<sup>+</sup> and Tl<sup>+</sup>, are practically insoluble in water or other polar solvents and possess high surface areas [25]. The higher surface area, mainly arising from microporosity observed for cesium salts with Cs/W ratio of >2 compensates the loss of acidic protons.

In literature, there is discussion about nature of acidic salts of heteropoly acids. It is supposed that in salts with number of counter ions (which replaces hydrogen ions)  $x < 2$ , acidic salt is a heterogeneous mixture of microporous neutral salt and unreacted acid; in salts with  $x > 2$  the salts are composed of grains with crystalline core of neutral salt covered by surface layer of unreacted acid [26–29].

Partial substitution of protons by these cations may result in changes of the number of available surface acidic sites. For example, the salt Cs<sub>2.5</sub>H<sub>0.5</sub>PW<sub>12</sub>O<sub>40</sub> was reported as superior catalyst which exhibit significantly higher activity than the parent acid in gas phase acid-catalyzed reactions [30]. However, the cesium salt of HPA forms colloidal suspension in polar media causing filtration problems. This drawback could be overcome by stabilizing Cs salt of HPA in a porous support.

For the preparation reasons a major disadvantage of HPAs salts with big cation consists in their insolubility which makes conventional aqueous impregnation on different supports impossible. For this reason, Soled et al. [13] used a sequential impregnation and in situ reaction on two types of supports: silica and  $\gamma$ -Al<sub>2</sub>O<sub>3</sub>.

Rao et al. studied Cs<sub>2.5</sub>H<sub>0.5</sub>PW<sub>12</sub>O<sub>40</sub> heteropolyacid salt prepared by the same technique by deposition of the parent salt on SBA-15 support. As Cs acid salts are insoluble, the SBA-15 supported Cs-acid salt was prepared by two-step sequential impregnation and in situ reaction on the support [16]. Silica supported ammonium salt of 12-molybdophosphoric acid catalysts has been investigated by Gong et al. on liquid nitration of benzene with 65% nitric acid as nitrating agent [31]. These catalysts with different loadings were prepared by sol–gel method and supported catalysts had high nitration reaction catalytic activity and selectivity over nitrobenzene.

Although different HPAs salts (especially of H<sub>3</sub>PW<sub>12</sub>O<sub>40</sub> acid) based on only one type of cation or mixed salts have been extensively reported, the influence of surface coverage of Cs salts of 12-molybdophosphoric supported on SBA-15 in reference to the bulk solid HPM have not been significantly explored in the literature.

In order to obtain highly dispersed heteropolyacid species, the Cs salt of molybdophosphoric acid Cs<sub>2.5</sub>H<sub>0.5</sub>PMo<sub>12</sub>O<sub>40</sub> (CsHPM) was supported on SBA-15 in the concentration of 20, 30 and 40 wt.% loading. The goal of this work was to characterise the texture, structure and the influence of surface coverage of these heteropolyacids salts in reference to the bulk solid heteropolyacids and to investigate their catalytic activity.

## 2. Experimental

### 2.1. Sample preparation

The bulk CsHPM with Cs/Keggin unit ratio of 2.5 was prepared by adding slowly drop wise the required amount of aqueous cesium nitrate CsNO<sub>3</sub> (0.267 g, 1.37 mmol) to aqueous H<sub>3</sub>PMo<sub>12</sub>O<sub>40</sub> (1 g, 0.55 mmol) with vigorous stirring at room temperature. The precipitate obtained was aged in parent solution for 24 h at room temperature, followed by evaporation in vacuum at 50 °C, and finally calcination at 300 °C for 4 h.

The Cs<sub>2.5</sub>H<sub>0.5</sub>PMo<sub>12</sub>O<sub>40</sub> (CsHPM) – SBA15 composites were prepared by incipient wetness technique. 8 g of precalcined SBA-15 was dried in oven at 120 °C for 3 h. For the preparation of 20CsHPM/SBA15 composite, 0.534 g (2.74 mmol) of CsNO<sub>3</sub> was weighed accurately and dissolved in 10 ml of ethanol. This volume of solvent used was approximately equal to the pore volume of the SBA15 support. The solution was added in small aliquots of 1 ml to the SBA-15 molecular sieve with constant stirring with a glass rod or kneading it properly. The solution was added at time intervals of 2 min. The formed paste was kneading for 20 min resulted in a free flowing powder. The resulted material was dried at 120 °C for the removal of solvents, and finally calcined at 300 °C.

After that, the obtained material was impregnated by 12-molybdophosphoric acid (2 g, 1.1 mmol) in 10 ml of ethanol. The solution was added to the treated SBA-15 molecular sieve by following the above procedure. The resulted composite was dried in an oven at 120 °C for 4 h and then calcined at 300 °C for 4 h.

The CsHPM was deposited in the concentration of 20, 30 and 40 wt.% concentration loadings.

Mesoporous silica SBA-15 was synthesized according to the procedure developed by Zhao et al. by the hydrolysis of tetraethyl orthosilicate (TEOS) using a P123 block copolymer as surfactant [32,33]. The synthesis was performed as follows: amphiphilic difunctional block copolymer, Pluronic P123 (4.6 g, 0.79 mmol) was dissolved in deionised water (125 g, 6.94 mol) and 2 M HCl solution (120 g, 3.29 mol) with stirring, at 40 °C. Then, TEOS (9.0 g, 43.20 mmol) was added to the solution with stirring at 40 °C for 24 h. The homogeneous gel mixture was then transferred into a Teflon flask, sealed and heated at 100 °C for 48 h. After

filtration and washing with water, the white solid product was air-dried at room temperature for 24 h. The sample was then calcined in air by a ramp of 1 °C/min to 540 °C and held at that temperature for 10 h.

The structure and texture of CsHPM supported on SBA-15 were studied by XRD, FT-IR and micro-Raman spectroscopy, SEM-EDX and low temperature nitrogen adsorption technique.

## 2.2. Measurements of textural properties

Textural characteristics of the outgassed samples were obtained from nitrogen physisorption using a Quantachrome instrument, Nova 2000 series. The specific surface area  $S_{\text{BET}}$ , average cylindrical pore diameters  $d_p$  and adsorption pore volume  $V_{\text{pN}_2}$  were determined. Prior to the measurements the samples were degassed to  $10^{-5}$  Pa at 250 °C. The BET specific surface area was calculated by using the standard Brunauer, Emmett and Teller method on the basis of the adsorption data. The pore size distributions were calculated applying the Barrett–Joyner–Halenda (BJH) method to the desorption branches of the isotherms. The IUPAC classification of pores and isotherms were used in this study.

## 2.3. XRD analysis

Powder X-ray diffraction data were obtained with a XD 8 Advanced Bruker diffractometer using the Cu K $\alpha$  radiation in the range  $2\theta = 0.5$ – $5^\circ$  at low angles and  $2\theta = 5$ – $60^\circ$ .

## 2.4. Surface characterization by fourier transform infrared (FT-IR) spectroscopy and micro-Raman spectroscopy

The FTIR absorption spectra were recorded with a Jasco 430 spectrometer (spectral range 4000–400  $\text{cm}^{-1}$  range, 256 scans, and resolution 2  $\text{cm}^{-1}$ ) using KBr pellets.

The micro-Raman spectra of polycrystalline samples were recorded on a Thermo DXR Raman microscope, using the 532 nm excitation line from a diode pumped, solid state laser, with a constant power of 5 mW and spot size of 0.7 m on the sample. The spectra were recorded using 25 m pinhole confocal aperture, with 10 s exposure and 10 repetitions. The spectral resolution of all the measured spectra was 2  $\text{cm}^{-1}$ . The data were collected at room temperature.

Raman mapping images were generated by measuring Raman spectra from areas of about 100  $\mu\text{m}^2$  in step sizes of 10  $\mu\text{m}$  (for 10  $\times$  10 probe spots). The sample was mounted on an automated XY translation stage controlled by a computer. The mapping was obtained by focusing the laser beam with 50 $\times$  magnification. The spatial resolution was 1  $\mu\text{m}$  and the size of the laser beam was 0.7  $\mu\text{m}$ .

## 2.5. Thermal analysis

Thermal analysis was carried out using a TGA/SDTA 851-LF 1100 Mettler apparatus. The samples with mass of about 100 mg were placed in alumina crucible of 900  $\mu\text{l}$ . The measurements were performed in dynamic air atmosphere with the flow rate of 50  $\text{mL min}^{-1}$ , in the temperature range of 25–700 °C with a heating rate of 10 °C  $\text{min}^{-1}$ . The air supplied by a compressor (4–5 bar) was passed over granular silica gel. The nitrogen was supplied from Linde gas cylinder (150 bar) of purity  $\geq 99.996\%$ .

DSC analysis was carried out with a Mettler Star system DSC 823 apparatus. The samples with mass of 20–40 mg were placed in Pt crucible of 150  $\mu\text{l}$ . The measurements were performed in dynamic air atmosphere with the flow rate of 50  $\text{mL min}^{-1}$ , in the temperature range of 30–650 °C with a heating rate of 10 °C  $\text{min}^{-1}$ .

## 2.6. Scanning electronic microscopy (SEM) and EDS analysis

Microstructure characterisation of the catalyst particles was carried out with a JEOL JSM-6610LV scanning electron microscope (SEM) connected with an INCA energy-dispersion X-ray analysis (EDX) unit with resolution of 0.126 keV. An acceleration voltage of 20 kV was used for the images. Powder materials were deposited on adhesive tape fixed to specimen tabs and then ion sputter coated with gold.

## 2.7. Catalytic properties

Catalytic conversion and selectivities were measured for vapour phase ethanol dehydration reaction at 250, 275 and 300 °C. A differential tubular stainless steel flow reactor, which was placed into a tubular furnace, was used for the gas phase ethanol dehydration reaction. Temperature of the reactor was controlled by a temperature controller within  $\pm 1\%$ . Before each experiment, 100 mg of the synthesized catalyst was placed in the middle of the stainless steel tubular reactor of 3/8 in. in diameter, and supported by quartz (0.2–0.5 mm) from both ends.

Liquid ethanol (99.8% Riedel de Haen) was pumped by a syringe pump at a flow rate of 1.2 ml/h into an evaporator where it is mixed with nitrogen and air to adjust the reactor feed composition. The evaporator was heated to 150 °C and kept at this temperature. Ethanol was mixed with nitrogen and air at a ratio of Et-OH:N $_2$ :O $_2$  = 1:3.5:0.4 in the evaporator. The total flow rate of the vapour stream was kept constant at 30 ml/min.

The composition of the reactor effluent stream was analyzed using a gas chromatograph (Hewlett Packard 5890 GC), which was equipped with a (FID) flame ionization detector. A Poropak QS column was used in the analysis of the product stream. The chromatograph was connected online to the reactor outlet. Using a temperature program (hold the temperature at 50 °C for 5 min, increase the temperature up to 200 °C with a heating rate of 20 °C/min and then hold the temperature for 12 min at 200 °C) in GC analysis, ethylene, acetaldehyde, ethanol and diethyl – ether peaks were observed at 3.93, 11.75, 12.93 and 15.65 min, respectively. All the connection lines were heated to 150 °C to prevent condensation.

The conversion of ethanol and selectivity were calculated as follows:

$$\text{Conversion} = \frac{\text{moles of ethanol reacted}}{\text{moles of ethanol in the feed}} \times 100 \quad (1)$$

Selectivity was calculated in carbon-based values:

$$\text{Selectivity} = \frac{\text{moles of product desired}}{\text{moles of reacted ethanol}} \times 100 \quad (2)$$

## 3. Results and discussion

### 3.1. Porosity and surface area

The N $_2$  adsorption–desorption isotherms of the parent mesoporous silica SBA 15 and CsHPM – SBA15 composites show a typical adsorption curve of type IV as defined by the IUPAC (Fig. 1). In the isotherms of SBA 15 and CsHPM – SBA15 composites, three stages can be identified (i) a slow increase in nitrogen uptake at low relative pressure, corresponding to monolayer–multilayer adsorption on the pores, (ii) a sharp step at intermediate relative pressure indication of capillary condensation in mesopores and (iii) a plateau at high relative pressure associated with multilayer adsorption on the external surface [34].

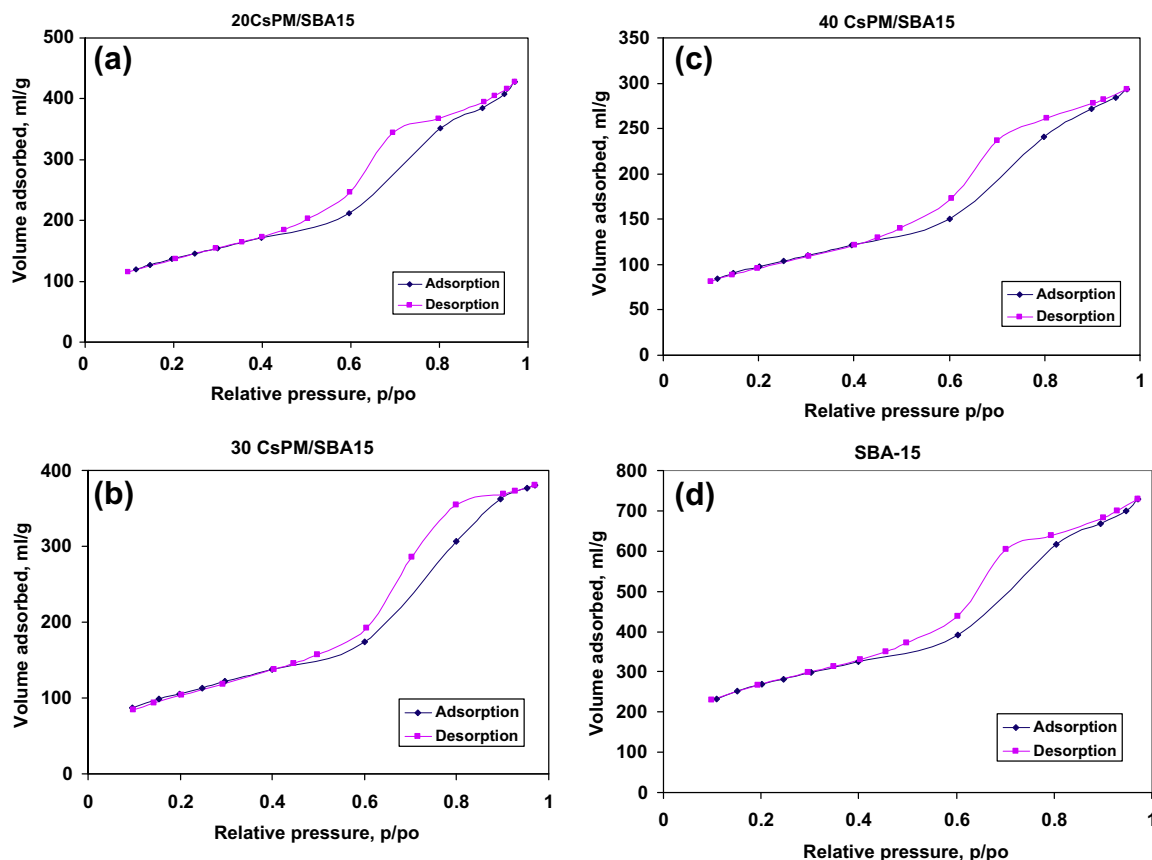


Fig. 1. Nitrogen adsorption–desorption isotherms of  $\text{Cs}_{2.5}\text{H}_{0.5}\text{PMo}_{12}\text{O}_{40}$  supported on SBA-15 at different wt.% loading: 20CsHPM-SBA-15 (a), 30CsHPM-SBA-15 (b) 40CsHPM-SBA-15 (c) and SBA-15 (d).

An obvious hysteresis loop at a relative pressure of  $p/p_0 = 0.4$ – $0.9$  is evidenced for the parent mesoporous silica SBA 15 and CsHPM – SBA15 composites. Hysteresis appearing in the multilayer range of physisorption isotherms is usually associated with capillary condensation in mesopore structures. The shapes of hysteresis loops have often been identified with specific pore structures. In our case the hysteresis type H1 is associated with porous materials known to consist of agglomerates or compacts of approximately uniform spheres in fairly regular array, and hence to have narrow distributions of pore size [34].

The specific surface area, pore volume and pore diameter determined from the isotherms using the BJH method are given in Table 1. For parent  $\text{Cs}_{2.5}\text{H}_{0.5}\text{PMo}_{12}\text{O}_{40}$  a narrow hysteresis loop is observed (not shown). The bulk  $\text{Cs}_{2.5}\text{H}_{0.5}\text{PMo}_{12}\text{O}_{40}$  salt displayed surface is of  $103 \text{ m}^2/\text{g}$  and a pore volume  $0.086 \text{ ml/g}$  that correspond to the average pore diameter of  $3.4 \text{ nm}$ .

The pore size distribution curves of parent mesoporous silica SBA 15 have narrow pore size distribution within mesopore range with a maximum at  $6.2 \text{ nm}$  (not shown). The pore size distribution

curves of CsHPM – SBA15 composites have one maximum within mesopore range between  $5.80 \text{ nm}$  for 40CsHPM – SBA15 and  $6.08 \text{ nm}$  in the case of 20CsHPM – SBA15.

Generally, after HPAs incorporation in different mesoporous silicas, the surface area, pore volume and pore diameter of samples decreased with increased concentration of active phase loading. Our results show that by impregnation of CsHPM onto SBA-15, its surface area is enhanced substantially, but the surface area decreases with increasing CsHPM loadings. However, the high surface area above  $450 \text{ m}^2/\text{g}$  could be retained for 20CsHPM-SBA15. The surface area, pore volume and pore diameter of CsHPM – SBA15 composites decreases with CsHPM loading due to the partial blockage of the mesopores of the support by CsHPM particles.

### 3.2. FTIR and Raman spectrometry

The effect of incorporation of heteropolyacids species and their surface coverage influence on SBA-15 matrix was studied by FT-IR and Raman spectrometry (Figs. 2 and 3) In order to confirm the presence of the Keggin anion on CsHPM – SBA15 composites, the samples were analysed by FTIR and Raman spectroscopy. The  $\text{PMo}_{12}\text{O}_{40}^{3-}$  Keggin ion structure consists of a  $\text{PO}_4$  tetrahedron surround by four  $\text{MoO}_3$  units formed by edge-sharing octahedra. These groups are connected each other by corner-sharing oxygen. This structure give rise to four types of oxygen, being responsible for the fingerprints bands of Keggin ion between  $1200$  and  $700 \text{ cm}^{-1}$ .

The parent  $\text{Cs}_{2.5}\text{H}_{0.5}\text{PMo}_{12}\text{O}_{40}$  show an IR spectrum containing the main vibrations at  $1066 \text{ cm}^{-1}$ ,  $970 \text{ cm}^{-1}$ ,  $867 \text{ cm}^{-1}$ ,  $793 \text{ cm}^{-1}$  assigned to the stretching vibrations  $\nu_{\text{as}} \text{P-O}_a$ ,  $\nu_{\text{as}} \text{Mo=O}_d$ ,  $\nu_{\text{as}} \text{Mo-O}_b\text{-Mo}$  and  $\nu_{\text{as}} \text{Mo-O}_c\text{-Mo}$  corresponding to the Keggin

Table 1  
Textural properties of  $\text{Cs}_{2.5}\text{H}_{0.5}\text{PMo}_{12}\text{O}_{40}$  – SBA15 composites.

Sample	Specific surface area ( $\text{m}^2/\text{g}$ )	Pore volume BJH <sub>Des</sub> (ml/g)	Average pore diameter BJH <sub>Des</sub> (nm)
Mesoporous silica SBA15	725	1.12	6.22
20CsHPM/SBA15	476	0.66	6.08
30CsHPM/SBA15	445	0.59	5.95
40CsHPM/SBA15	397	0.45	5.80
CsHPM	103	0.086	3.4



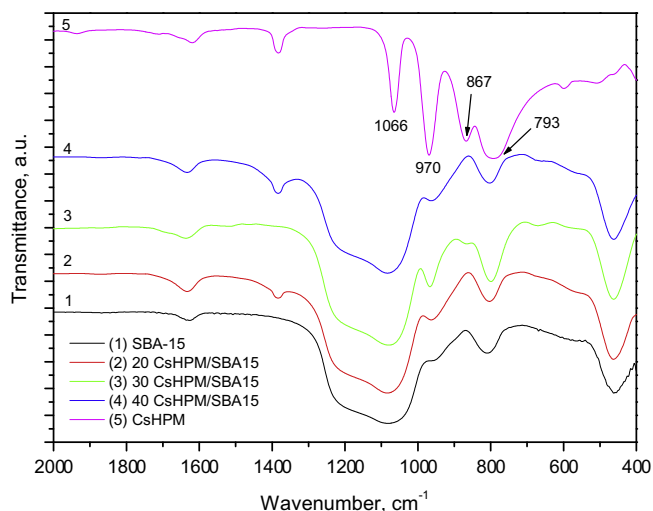


Fig. 2. FTIR spectra of CsHPM – SBA15 composites.

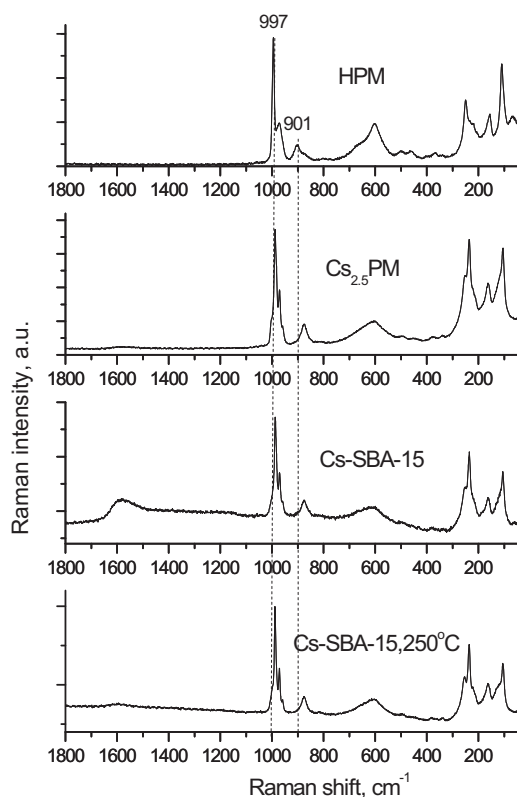


Fig. 3. Raman spectra of  $\text{H}_3\text{PMoO}_{40}$  (HPM),  $\text{Cs}_{2.5}\text{H}_{0.5}\text{PMoO}_{40}$  (CsHPM), SBA-15 loaded with  $\text{Cs}_{2.5}\text{H}_{0.5}\text{PMoO}_{40}$ , 20 wt.% (20CsHPM-SBA-15) and 20CsHPM-SBA-15 calcinated at 250 °C.

structure [35,36]. Some of these bands are preserved on the supported samples, but they are broadened and partially obscured because of the strong absorption bands of silica from SBA-15 (1090, 800 and 465  $\text{cm}^{-1}$ ) (Fig. 2).

The introduction of Cs salt of HPM heteropolyacid into the SBA-15 matrix slightly influenced the structure of resulted composites. The bands of CsHPM supported on SBA-15 in the 1300–400  $\text{cm}^{-1}$  region are partially or completely overlapped by the bands of the silica matrix. The band assigned to the P–O asymmetric stretching vibration at 1064  $\text{cm}^{-1}$  is completely overlapped by the strong

band at 1090  $\text{cm}^{-1}$  of the silica. One strong band in the spectra of CsHPM – SBA-15 composites appeared at 968  $\text{cm}^{-1}$  which correspond to  $\nu_{\text{as}} \text{Mo}=\text{O}_d$  vibration band of pure HPM. Also a band with moderate intensity was observed at 867  $\text{cm}^{-1}$  which corresponds to the  $\nu_{\text{as}} \text{Mo}-\text{O}_c-\text{Mo}$  vibration of the HPM.

The Raman spectrum of HPM is in accordance with the previously published results [37]. When protons are replaced by large cation such as Cs changes in the structure are evidenced by changes in Raman spectrum. There is slight shift of the main bands towards lower frequencies in the case of CsHPM related to parent acid. The Keggin structure is preserved but the main characteristic features of the structure are observed at 988  $\text{cm}^{-1}$  ( $\nu_s \text{Mo}-\text{O}_d$ ), 971  $\text{cm}^{-1}$  ( $\nu_{\text{as}} \text{Mo}-\text{O}_d$ ), 875  $\text{cm}^{-1}$  ( $\nu_{\text{as}} \text{Mo}-\text{O}_b-\text{Mo}$ ), 600  $\text{cm}^{-1}$  ( $\nu_s \text{Mo}-\text{O}_c-\text{Mo}$ ), 381  $\text{cm}^{-1}$ , 336  $\text{cm}^{-1}$ , 235  $\text{cm}^{-1}$  ( $\nu_s \text{Mo}-\text{O}_a$  with an important bridge stretching character according to Ref. [37]), at 164 and 105  $\text{cm}^{-1}$ .

The spectra of pure salt CsHPM and SBA-15 loaded with CsHPM have no mutual differences except appearance of the broad band about 1600  $\text{cm}^{-1}$  which originates from water adsorbed in micropore structure of molecular sieve (Fig. 3). As SBA-15 have no characteristic Raman signature, it is obvious that CsHPM is supported in microstructure of SBA-15 without changes in its primary Keggin structure. After thermal treatment at 250 °C, the Raman spectrum of SBA-15 loaded with salt CsHPM shows only slight modifications; the Raman signals are slightly sharper which can be a consequence of higher crystallinity of the composite while band about 1600  $\text{cm}^{-1}$  completely disappears after calcination.

Raman mapping can provide molecular information to complement data derived from other analytical techniques. Two dimensional or three dimensional distributions of various chemical species present in sample can be obtained, which means that it is possible to get chemical composition of different structural parts, as evident in SEM images. In Fig. 4 a photograph of selected area of sample CsSBA-15 is presented with a grid (90 × 90  $\mu\text{m}$ ). At each point, the Raman spectrum was recorded with exposed time of 7 s, number of exposures 5 and power of 5 mW at sample.

To develop the maps of CsHPM-SBA, the intensity of bands at 988  $\text{cm}^{-1}$  due to symmetric stretching  $\text{Mo}-\text{O}_d$  and 235  $\text{cm}^{-1}$  due to symmetric  $\text{Mo}-\text{O}_a$  modes were employed. The mapping images of SBA-15 were obtained by using the water molecule bending mode at about 1600  $\text{cm}^{-1}$ . The detailed analysis of 100 Raman spectra recorded for each sample have shown that Keggin anion was the only structure incorporated into the SBA-15. No lacunary Keggin or other structures were identified. The average Raman spectra of SBA-15 loaded with 20% and 40% of CsHPM in Fig. 5 show main characteristics of Keggin structure. As can be seen, in the case of 40CsHPM-SBA15 composite with higher content of CsHPM, the fluorescence is more expressed.

Maps of CsHPM-SBA15 with 20 and 40 wt.% of salt loaded are presented in Fig. 6a and c while maps of SBA-15 molecular sieve are given for comparison in Fig. 6b and d. It can be observed that distribution of CsHPM salt over the surface is more homogeneous in the case of 20% loading. In the case of 40% of salt loading, the dispersion of the salt over the molecular sieve surface is worse; the salt is forming separated islands over the SBA-15 surface, which means that salt starts to aggregate on the pore walls of SBA-15.

### 3.3. X-ray diffraction

The XRD patterns at low angles for the initial mesoporous silica SBA15 show three diffraction peaks below  $2.0^\circ (2\theta)$  (Fig. 7), indicating its well-ordered two-dimensional mesostructure [32]. It is shown that the peaks at low angles assigned to SBA-15 appear for CsHPM – SBA15 composites with different CsHPM loadings, indicating that they keep the mesopore structure well, with well dispersed CsHPM on the surface of pore walls of SBA-15.

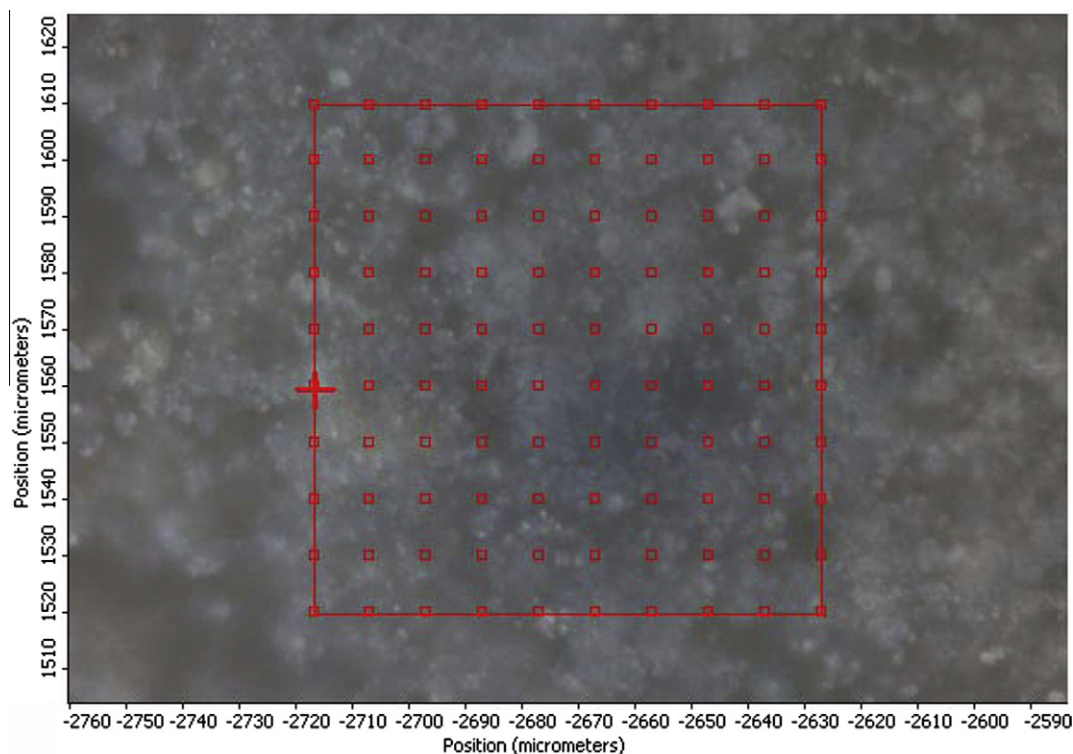


Fig. 4. Photograph of selected area of CsPM-SBA-15 with grid selected for mapping.

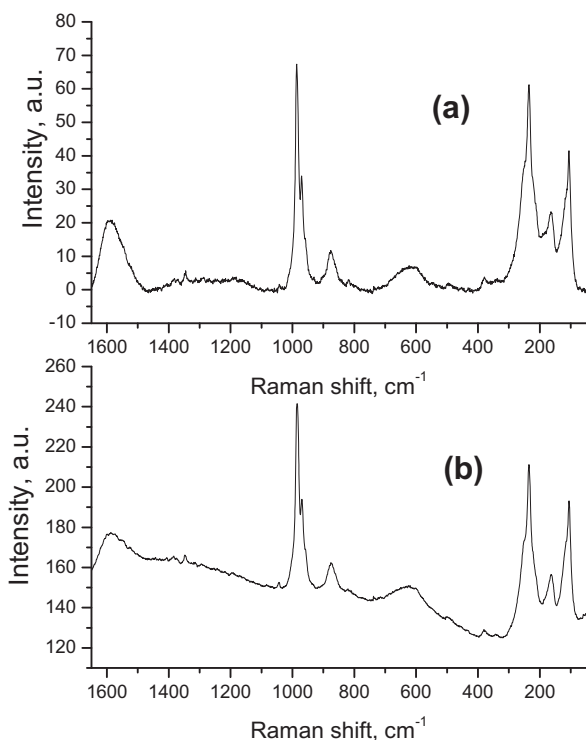


Fig. 5. Average Raman spectra recorded in selected areas (without background correction) of: (a) CsHPM-SBA-15, 20 wt.% and (b) CsHPM-SBA-15, 40 wt.%.

For the CsHPM – SBA15 composites the diffraction peaks at low angles are presented but with diminished intensity and slightly shifted to higher angles values. As with increasing loading of active phase, the intensity of diffraction picks are more diminished it can be supposed that the decrease in the intensity may be related to

the presence of interfering scattering due to the presence of CsHPM. Also, it can be asserted that the long – range order of mesoporous silica is decreased more evidently for a higher loading of 40 wt.% CsHPM.

### 3.4. Thermal analysis

As in the case of parent HPM, the main processes observed during the thermal treatment of pure CsHPM are: the crystallisation water elimination in several steps, the decomposition of the anhydrous acids by constitutive water removal (all accompanied by endothermic effects) and finally the crystallisation process of constitutive oxides accompanied by exothermic effects [38,39].

In the region of the hydrated water elimination, the DTA curve of bulk CsHPM shows two endothermic peaks at 59.5 and 97 °C (not shown), which may be assigned to bonded water from the crystal hydrates with different number of water molecules [38]. From TG and DTG curves it could be observed the loss of water of crystallisation processes accompanied by a considerable weight loss. The final process evidenced by an exothermic peak over 500 °C is assigned to the destruction of Keggin structure and crystallisation of constitutive oxides:  $\text{MoO}_3$  and  $\text{P}_2\text{O}_5$ .

For all CsHPM – SBA15 composites from TG, DTG and DTA thermal curves, one can see a different behaviour in comparison with pure CsHPM in the temperature range corresponding to the elimination of the hydrated water due to composites higher specific surface area (Table 1).

In the case of 20CsHPM – SBA15 composite the first endothermic effect (68 °C) is due to the additive thermal effects of the desorbed water from silica surface and to the loss of the first part of the HPA crystallisation water (Fig. 8). The second endothermic effect appears at 88 °C and is due to the loss of the second part of the crystallisation water. The loss of the hydrated water is completed up to 150 °C.

In the temperature range 150–450 °C a slow and continuous loss of sample weight is proceeding, owing to the departure of

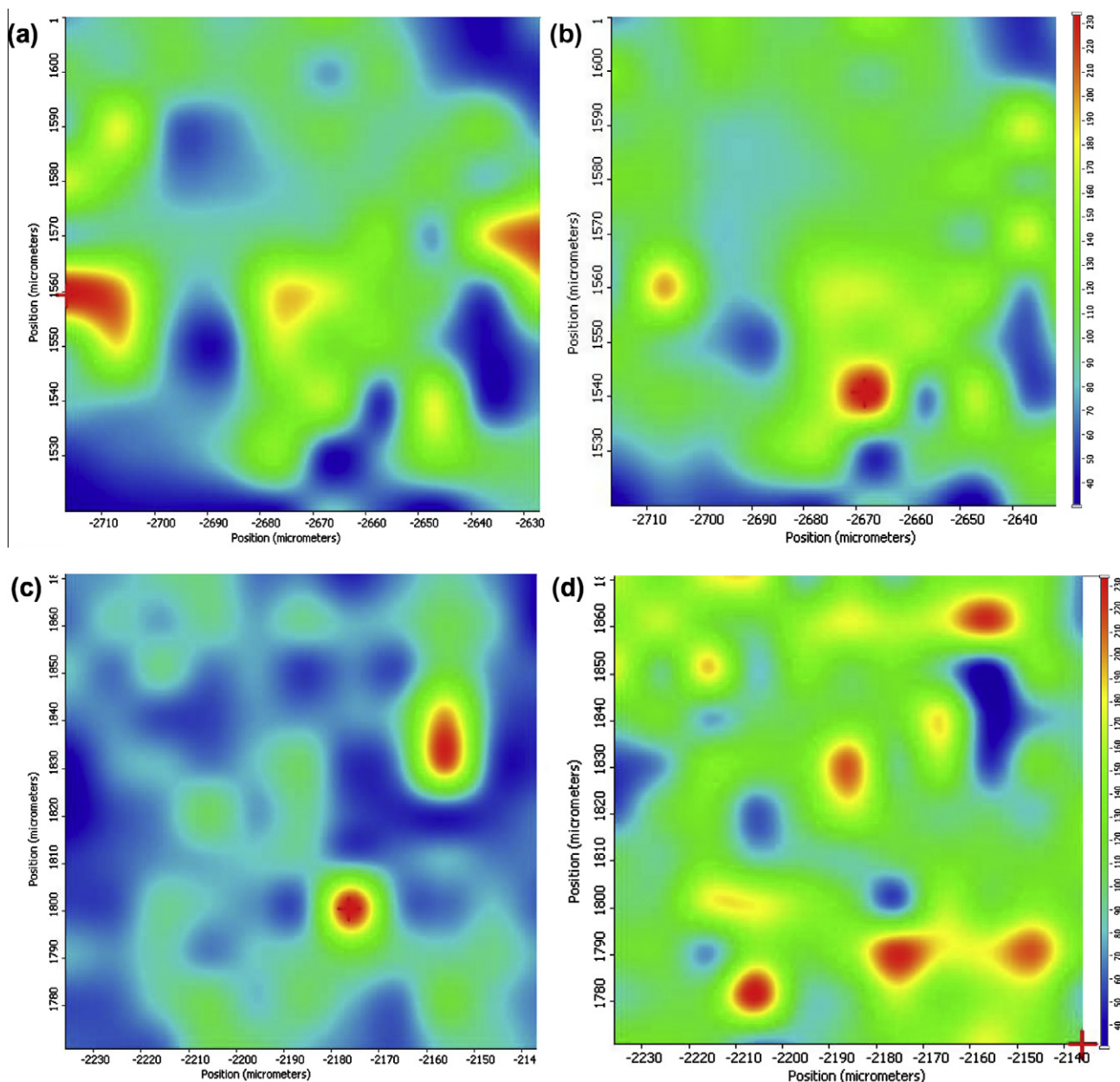


**Fig. 6.** Raman mapping of: (a) M–O<sub>d</sub> band at 988 cm<sup>−1</sup> and (b) O–H band at 1640 cm<sup>−1</sup> of CsHPM-SBA15 composite with 20 wt.% CsHPM and (c) M–O<sub>d</sub> band at 988 cm<sup>−1</sup> and (d) O–H band at 1640 cm<sup>−1</sup> of CsHPM-SBA15 composite with 40 wt.% CsHPM. The colour scale situated at right of the Raman mappings represents the intensity in arbitrary units.

water molecules of the CsHPM and probably to remaining traces of the organic surfactant used for preparation of mesoporous SBA15. The constitutional water – which is formed from acidic protons and oxygen belonging to the Keggin units – are removed between 450 and 550 °C temperature range, this process being evidenced on DTG curve at 478 °C.

For all CsHPM – SBA15 composites an exothermic peak could be observed on DTA curve at a temperature higher than 600 °C. This exothermic peak could be assigned to the decomposition of active phase CsHPM and crystallisation of constitutive oxides resulted after decomposition.

The decomposition of pure CsHPM and all CsHPM – SBA15 composites is better evidenced by DSC method. For 20CsHPM-SBA15 the exothermic peak assigned to the decomposition of active phase is observed at 625 °C, while for the other compositions this peak is observed at 623 °C (30CsHPM-SBA15) and respectively at 597 °C

for 40CsHPM-SBA15 composite (Fig. 9). Pure CsHPM is thermally less stable, the exothermic peak being observed at 506 °C on DSC curve. Therefore immobilization on mesoporous SBA-15 obviously increases the thermal stability of the Keggin structures in comparison with their parent bulk Cs salts, probably related with the interaction of CsHPM with surface silanols on the support.

### 3.5. SEM and EDS characterization

The morphology of CsHPM – SBA15 composites is very similar with SBA 15 support. It is composed of rope like shape particles with an average diameter below 1 μm (Fig. 10).

The diameter size of the ropes is relatively uniform, and the ropes can be aggregated into wheat like macroscopic structures. CsHPM distribution over the surface of SBA-15 was analysed by SEM-EDS method. In order to get representative composition a



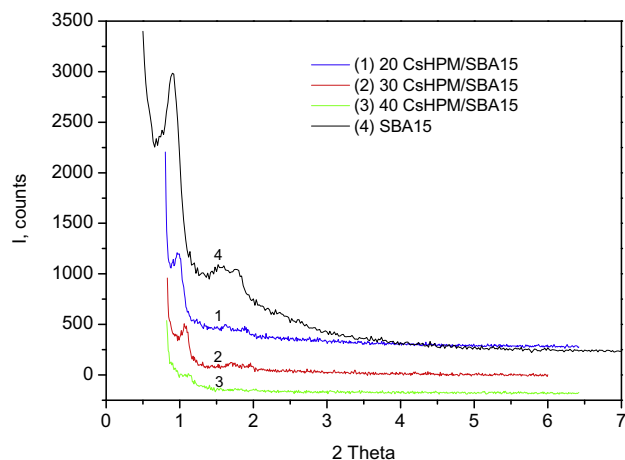


Fig. 7. X-ray diffraction pattern of CsHPM – SBA15 composites.

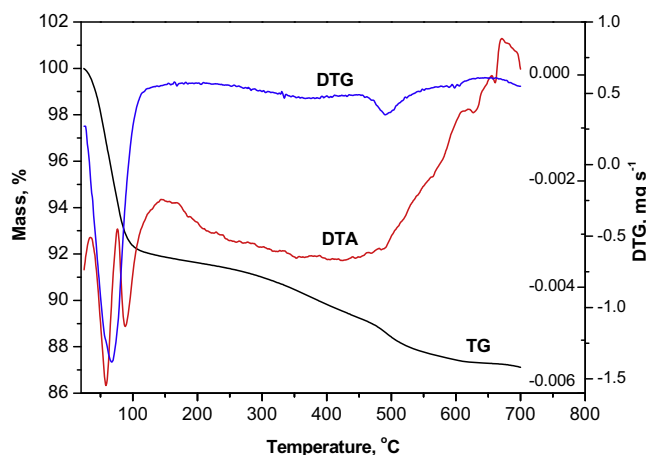


Fig. 8. TG-DTG and DTA curves of 20CsHPM – SBA15 composites.

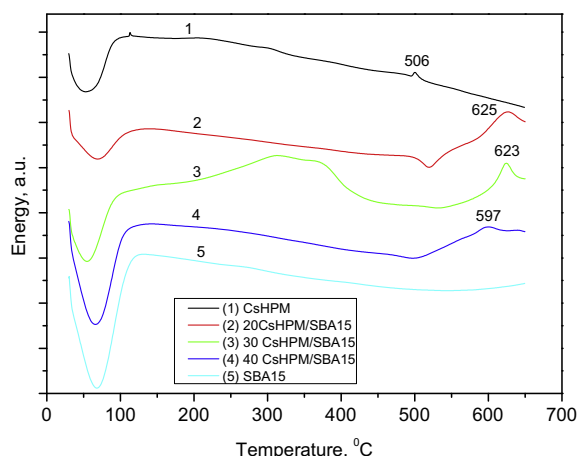


Fig. 9. DSC analysis of CsHPM – SBA15 composites.

minimum of four areas of about  $500 \times 500 \mu\text{m}$  were analyzed on each sample. An example of selected areas and corresponding EDS spectrum are presented in Fig. S1, a and b (given in Supplementary Material). The analysis was repeated on different particles of the same batch in order to ensure the reproducibility of the obtained results.

By this technique was obtained the chemical composition of silicon from SBA-15 and Mo, P and Cs elements of salt from CsHPM – SBA15 composites.

The data of EDS analysis for  $\text{Cs}_{2.5}\text{H}_{0.5}\text{PMo}_{12}\text{O}_{40}$  – SBA15 composites show that the molybdenum, phosphorous and cesium content is relatively homogeneous and close to stoichiometric values.

In the case of uncalcined 20CsHPM/SBA-15 composites the average content of Mo as wt.% is quite the same as stoichiometric one: 10.94 is experimental value and stoichiometric value is 10.9 wt.%. Also, P content (0.23 wt.%) and Cs content (3.20 wt.%) are close to stoichiometric values (Table 2). For the same composite after calcination at 250 °C the content of Mo is a little more than stoichiometric value: 11.14 wt.% is experimental value, while the content of Cs (3.06 wt.% is experimental value) is a little less than stoichiometric value.

Comparing the experimental and stoichiometric values of Mo and Cs concentration values, it can be observed that for higher loadings of active phase (30% and 40%), the samples exhibit some small deviations, for both non-calcinated and calcinated ones. It could be supposed that active phase was less homogeneously dispersed inside the composites pores than for low loadings of active phase, which is in accordance with Raman spectra mapping results.

### 3.6. Results of ethanol dehydration reactions

The dehydration of ethanol was used to probe the catalytic properties of the CsHPM samples incorporated on the silica matrix. Catalytic activity of the synthesized CsHPM–silica-based nanocomposite catalysts for vapour phase ethanol dehydration reaction was tested in a fixed bed flow reactor described in the experimental section.

During the experiments, at least three measurements were made at the same conditions. The data points reported in the conversion and the selectivity figures reported here correspond to the average of these three measurements. Results were highly reproducible and the activities of the catalysts did not change during the experiments.

The main reaction products obtained on acid (dehydration) catalytic centres were ethylene (ET) and diethyl ether (DEE), and respectively acetaldehyde (ACA) which was obtained on redox (dehydrogenation) catalytic centres. Ethylene and DEE are due to dehydration reactions occurred on the acid sites of the catalyst, while acetaldehyde formation through a dehydrogenation reaction indicated the presence of basic sites. In the effluent leaving the reactor were detected also unreacted alcohol and minor quantities of  $\text{CO}_x$ .

#### 3.6.1. Effect of CsHPA/silica ratio

Ethanol conversion over pure CsHPM and 40CsHPM – SBA15 catalysts has relatively constant values during the time on stream but values of conversion are higher for supported sample. For 20CsHPM – SBA15 and 30CsHPM – SBA15 -supported catalysts the values of ethanol conversion are lower in comparison with pure CsHPM ones and a continuing decrease of them with time on stream is evidenced (Fig. 11).

The CsHPM–silica-based nanocomposite catalysts synthesized here were found to be very efficient for ethylene formation from ethanol. The highest ethylene yield values were obtained with CsHPM and 40CsHPM – SBA15 catalysts. With these catalysts, selectivity of ethylene has values of around 75–85% obtained at reaction temperature of 300 °C.

Ethylene selectivity for pure CsHPM and 40CsHPM – SBA15 catalysts has relatively constant values during the time on stream (as in the case of Et-OH conversion) but values of ET selectivity are higher for CsHPM sample (see Fig. S2 in Supplementary material).

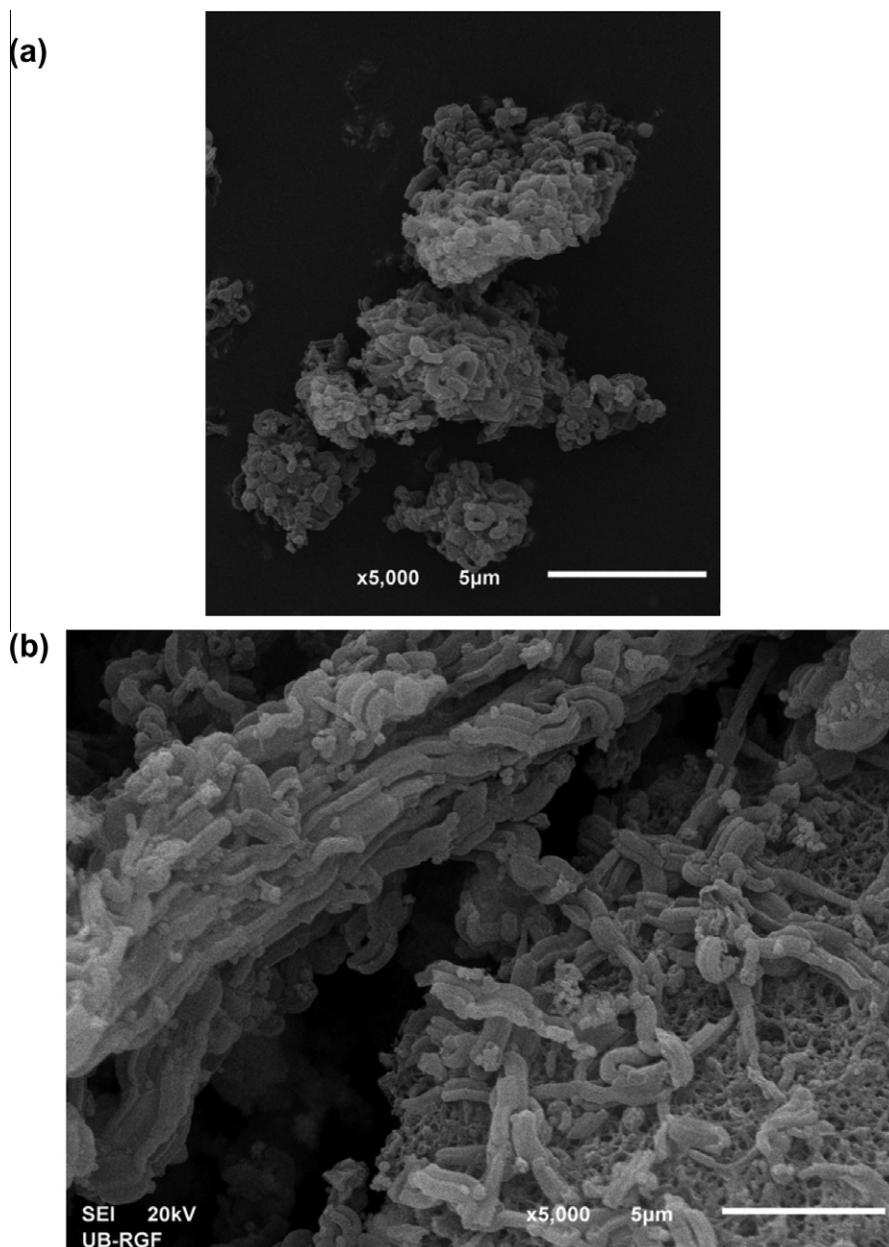


**Fig. 10.** SEM micrographs of 20 wt.% CsHPM-SBA15 (a) and 30 wt.% CsHPM – SBA15 composites (b).

**Table 2**

Energy dispersive X-ray (EDS) analysis data for Cs, P and Mo in  $\text{Cs}_{2.5}\text{H}_{0.5}\text{PMo}_{12}\text{O}_{40}$  – SBA15 composites, initial solids and solids obtained after calcination at 250 °C.

Sample	Elemental analysis (wt.%)					
	Mo		P		Cs	
	Exp.	Stoich.	Exp.	Stoich.	Exp.	Stoich.
20CsHPM/SBA-15	10.94	10.9	0.23	0.29	3.20	3.15
30CsHPM/SBA-15	16.76	16.35	0.43	0.44	4.68	4.72
40CsHPM/SBA-15	22.05	21.8	0.60	0.59	6.18	6.29
20CsHPM/SBA-15_250 °C	11.14	10.9	0.25	0.29	3.06	3.15
30CsHPM/SBA-15_250 °C	16.51	16.35	0.39	0.44	4.55	4.72
40CsHPM/SBA-15_250 °C	20.93	21.8	0.54	0.59	6.14	6.29

For 20CsHPM – SBA15 and 30CsHPM – SBA15 -supported catalysts the values of ET selectivity are lower in comparison with pure CsHPM ones. A continuing decrease of the ET selectivity with time on stream could be seen, this tendency being very similar with the decreasing of ET-OH conversion. So, after reaction for 500 min, the

ethylene yields over 20CsHPM – SBA15 and 30CsHPM – SBA15 at 300 °C reached 32% and 58%, respectively.

The DEE selectivity increased with time on stream for 20CsHPM – SBA15 and 30CsHPM – SBA15 -supported catalysts while for pure CsHPM and 40CsHPM – SBA15 catalysts remain nearly constant

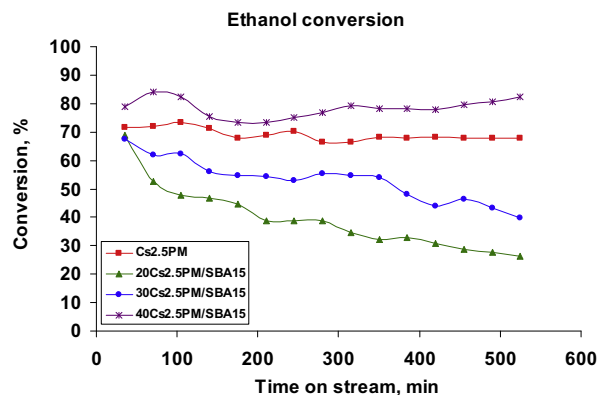


Fig. 11. Ethanol conversion values obtained with pure CsHPM and CsHPM – SBA15 composites at 300 °C.

with the increasing of time on stream (see Fig. S3 in Supplementary material). The values of DEE selectivity for 20CsHPM – SBA15 reach the maximum values after 5 h and then remain almost constant.

The third main product obtained in the catalyst test experiments was acetaldehyde. As shown in Fig. S4 (Supplementary material), acetaldehyde formation was observed in selectivity below 20%. Among the catalysts tested, highest acetaldehyde selectivities were obtained with 20CsHPM – SBA15 catalysts tested at 300 °C. Acetaldehyde (ACA) which is known to be produced on redox centres resulted in significant amount especially on supported catalysts in comparison with pure CsHPAs ones. However, supported 20CsHPM – SBA15 led to higher quantities of ACA, especially after 5 h on stream.

Thus, the very high dispersion of the HPAs on high surface area molecular sieve yielded an active catalyst for ethanol conversion and for acetaldehyde formation. The acetaldehyde selectivity increased gradually with time on stream from 5% to 17% in the case of 20CsHPM – SBA15.

Varisli et al. were reported a comparison of activities of three different pure heteropolyacid catalysts, namely  $H_3PW_{12}O_{40}$ ,  $H_3PMo_{12}O_{40}$  and  $H_4SiW_{12}O_{40}$  in the ethanol dehydration reaction. Among these three solid acid catalysts  $H_4SiW_{12}O_{40}$  showed the highest activity, but authors studied only the dehydration route of ethanol (Ethylene and DEE formation) and the dehydrogenation route (ACA formation) was not studied even for HPM [40]. In other paper Varisli et al. [41] were reported the ethanol dehydration reaction on a water insoluble W-silicate-based mesoporous nanocomposite catalyst, containing a high W/Si molar ratio. For these catalysts formation of some low yield of acetaldehyde was observed at reaction temperatures lower than 280 °C. The main products of ethanol dehydration reaction were ethylene and DEE and ethylene selectivity values approached to 100% over 260 °C with this catalyst. In a recent paper, a series of Mo/HZSM-5 catalysts were tested on ethanol dehydration reaction by Han et al. [42]. Mo/HZSM-5 calcined at 500 °C gave the best catalytic performance both in activity and ethylene selectivity. After reaction for 10 h, the ethylene yields over the catalyst reached 67%, which is a value close to the values of ET selectivity obtained on CsHPM /SBA-15 composites.

So, it could be concluded that ethylene formation on the acid sites of catalysts is favoured on W based HPAs, while acetaldehyde formation through a dehydrogenation reaction on basic sites is favoured on Mo based HPAs.

### 3.6.2. Effect of reaction temperature

Fig. S5 (Supplementary material), shows steady-state ethanol dehydration/dehydrogenation rates obtained for 20CsHPM – SBA15 samples as a function of time on stream in the temperature

range 250–300 °C. The dehydration rates are calculated as moles of reactant converted per minute per square meter of the surface area of CsHPM-SBA15 composite. Catalytic activity increased with increasing reaction temperature.

From a detailed analysis of Fig. S5 (Supplementary material), it is clear that ethanol dehydration rates seem to be strongly influenced by the temperature. When the reaction take place at 300 °C, at the beginning of the reaction, reaction rates are higher than 60 mmol of Et-OH converted per minute per square meter of the surface area of CsHPM. After 5–6 h the reaction rate decreased at 35 mmol of Et-OH/m<sup>2</sup> min and subsequently remained almost constant with time on stream. For catalytic tests at 250 and 275 °C the values of ethanol dehydration rates are below 30 mmol of Et-OH/m<sup>2</sup> min, but remained almost constant with time on stream during the experiment.

Fig. S6 (Supplementary material), shows the rates obtained for the ethylene formation reaction over the same supported 20CsHPM – SBA15 catalysts. Again, we find that the activity is dependent on the temperature. Also, the relative activity of these catalysts for ethylene formation follows the same tendency as observed in the case of ethanol dehydration.

Furthermore, Fig. S6 also indicates that the catalysts show more rapid decreasing of ethylene formation at 300 °C as after 6 h the values of reaction rates are similar with the ones observed at 275 °C. For all three temperature used in catalytic tests, the evolution of ethylene formation rates after 6 h remained almost constant with time on stream during the experiment.

The reaction rates for the other reaction products DEE and ACA over supported 20CsHPM – SBA15 catalysts increase with increasing reaction temperature.

For catalytic tests at 300 °C, the values of DEE reaction rates reach maximum values after 4 h and then remain almost constant, while for catalytic tests at 250 and 275 °C reaction rate values are constant during the experiment.

As was mentioned before, among the catalysts tested, highest ACA selectivities were obtained with 20CsHPM – SBA15 catalysts tested at 300 °C. Also, reaction rates for ACA formation have the highest values at 300 °C test. During the experiments values of reaction rates for ACA remain almost constant for all three testing temperature: 250, 275 and 300 °C.

## 4. Conclusions

In this study is described a procedure for supporting insoluble Cs acid salts on mesoporous SBA-15 by two-step sequential impregnation with a variation of active phase content (20–40 wt.%).

The presence of a low angle diffraction peaks and a high surface area of CsHPM/SBA-15 composites demonstrates that these materials have a mesoporous structure. However, from XRD patterns of CsHPM – SBA15 composites it can be asserted that the long – range order of mesoporous SBA-15 is decreased especially for high loading of 40 wt.% CsHPM.

FTIR and micro-Raman spectroscopy showed that CsHPM retained its parent Keggin structure after supporting into the substrate. From Raman mapping it can be observed that distribution of CsHPM salt over the surface of mesoporous SBA-15 is more homogeneous in the case of 20 wt.% salt loading, while for 40 wt.% loading, the salt is forming separated islands over the support surface.

From SEM-EDS analysis it could be observed that for higher loadings of active phase the samples exhibit some small deviations of Mo and Cs concentration values from the stoichiometric ones.

The ethanol conversion proceeds by two main pathways: an oxidehydrogenation reaction on redox catalytic centres, and a dehydration reaction on acidic centres, respectively. Parent CsHPM

and CsHPM – SBA15 composites have showed both acidic and redox properties and therefore the reaction products obtained are ethylene and DEE on acidic centres and acetaldehyde on redox catalytic centres, respectively. Anyway, the favourable effect of CsHPM deposition into the silica pores for oxidehydrogenation pathway to acetaldehyde results from the higher values of ACA selectivity especially for 20CsHPM – SBA15 composites.

## Acknowledgements

These investigations were partially financed by Romanian Academy Project No. 3.3 and the Serbian Ministry of Sciences, Grant 172043.

## Appendix A. Supplementary data

Supplementary data associated with this article can be found, in the online version, at [doi:10.1016/j.micromeso.2012.02.030](https://doi.org/10.1016/j.micromeso.2012.02.030).

## References

- [1] N. Mizuno, M. Misono, *Chem. Rev.* 98 (1998) 199–217.
- [2] F. Cavani, *Catal. Today* 41 (1998) 73–86.
- [3] A. Popa, V. Sasca, J. Halasz, *Appl. Surf. Sci.* 255 (5) (2008) 1830–1835.
- [4] G.D. Yadav, G. George, *Catal. Today* 141 (2009) 130–137.
- [5] Q.Y. Liu, W.L. Wu, J. Wang, X.Q. Ren, Y.R. Wang, *Micropor. Mesopor. Mater.* 76 (2004) 51–60.
- [6] R. Palcheva, A. Spojakina, L. Dimitrov, K. Jiratova, *Micropor. Mesopor. Mater.* 122 (2009) 128–134.
- [7] A. Popa, V. Sasca, E.E. Kiss, R. Marinkovic-Neducin, M.T. Bokorov, I. Holclajtner-Antunović, *Mater. Chem. Phys.* 119 (3) (2010) 465–470.
- [8] A. Popa, V. Sasca, E.E. Kiss, R. Marinkovic-Neducin, I. Holclajtner-Antunović, *Mater. Res. Bull.* 46 (2011) 19–25.
- [9] A. Popa, V. Sasca, E.E. Kiš, R. Marinkovic-Neducin, J. Halasz, *J. Optoelectron. Adv. Mater.* 10 (6) (2008) 1401–1407.
- [10] A. Popa, N. Plešu, V. Sasca, E.E. Kiš, R. Marinković-Nedućin, *J. Optoelectron. Adv. Mater.* 8 (5) (2006) 1944–1950.
- [11] N. Mizuno, M. Misono, *Chem. Lett.* (1987) 967–970.
- [12] N. Essayem, G. Coudurier, M. Fournier, J.C. Védrine, *Catal. Lett.* 34 (1995) 223–235.
- [13] S. Soled, S. Miseo, G. McVicker, W.E. Gates, A. Gutierrez, J. Paes, *Catal. Today* 36 (1997) 441–480.
- [14] A. Molnar, C. Keresszegi, B. Torok, *Appl. Catal. A: General* 189 (1999) 217–224.
- [15] A. Kukovecz, Zs. Balogi, Z. Konya, M. Toba, P. Lentz, S.-I. Niwa, F. Mizukami, A. Molnar, J.B. Nagy, I. Kiricsi, *Appl. Catal. A: General* 228 (2002) 83–94.
- [16] P.M. Rao, M.V. Landau, A. Wolfson, A.M. Shapira-Tchelet, M. Herskowitz, *Micropor. Mesopor. Mater.* 80 (2005) 43–55.
- [17] A. Molnar, T. Beregszaszi, A. Fudala, P. Lentz, J.B. Nagy, Z. Konya, I. Kiricsi, *J. Catal.* 202 (2001) 379–386.
- [18] J.S. Santos, J.A. Dias, S.C.L. Dias, F.A.C. Garcia, J.L. Macedo, F.S.G. Sousa, L.S. Almeida, *Appl. Catal. A: General* 394 (2011) 138–148.
- [19] C. Yuan, J. Chen, *Chin. J. Catal.* 32 (2011) 1191–1198.
- [20] X. Sheng, Y. Zhou, Y. Zhang, M. Xue, Y. Duan, *Chem. Eng. J.* 179 (2012) 295–301.
- [21] L. Yang, Y. Qi, X. Yuan, J. Shen, J. Kim, *J. Mol. Catal. A: Chemical* 229 (1–2) (2005) 199–205.
- [22] L. Lizama, T. Klimova, *Appl. Catal. B: Environ.* 82 (2008) 139–150.
- [23] A.I. Tropecêlo, M.H. Casimiro, I.M. Fonseca, A.M. Ramos, J. Vital, J.E. Castanheiro, *Appl. Catal. A: General* 390 (2010) 183–189.
- [24] R. Wei, M. Guo, J. Wang, *Chinese J. Chem. Eng.* 17 (1) (2009) 58–63.
- [25] J.B. Moffat, *Metal-Oxygen Clusters: The Surface and Catalytic Properties of Heteropoly Oxometalates*, Springer, New York, 2001.
- [26] J. Haber, L. Matachowski, D. Mucha, J. Stoch, P. Sarv, *Inorg. Chem.* 44 (2005) 6695–6703.
- [27] M. Misono, *Chem. Commun.* 13 (2001) 1141–1152.
- [28] P.Y. Gayraud, N. Essayem, J. Vedrine, *Catal. Lett.* 56 (1998) 35–41.
- [29] I. Holclajtner-Antunovic, U.B. Mioc, M. Todorovic, Z. Jovanovic, M. Davidovic, D. Bajuk-Bogdanovic, Z. Lausevic, *Mater. Res. Bull.* 45 (2010) 1679–1684.
- [30] I.V. Kozhevnikov, *Catalysis for Fine Chemical Syntheses – Catalysis by Polyoxometalates*, vol. 2, John Wiley & Sons, Ltd., Chichester, 2002.
- [31] S. Gong, L. Liu, Q. Cui, J. Ding, J. Hazard, *Mater. Res.* 178 (2010) 404–408.
- [32] D. Zhao, J. Feng, Q. Huo, N. Melosh, G.H. Fredrickson, B.F. Chmelka, G.D. Stucky, *Science*, 279 (1998) 548–552.
- [33] D. Zhao, J. Sun, Q. Li, G.D. Stucky, *Chem. Mater.* 12 (2000) 275–279.
- [34] K.S.W. Sing, D.H. Everett, R.A.W. Haul, L. Moscou, R.A. Pierotti, J. Rouquerol, T. Siemieniowska, *Pure Appl. Chem.* 57 (1985) 603–619.
- [35] A.J. Bridgeman, *Chem. Phys.* 287 (2003) 55–69.
- [36] C. Rocchiccioli-Deltcheff, M. Fournier, R. Frank, R. Thouvenot, *Inorg. Chem.* 22 (1983) 207–216.
- [37] C. Rocchiccioli-Deltcheff, A. Aouissi, M.M. Bettahar, S. Launay, M. Fournier, *J. Catal.* 164 (1996) 16–27.
- [38] V. Sasca, M. Stefanescu, A. Popa, *J. Therm. Anal. Cal.* 56 (1999) 569–578.
- [39] A. Popa, V. Sasca, M. Stefanescu, E.E. Kis, R. Marinkovic-Neducin, *J. Serb. Chem. Soc.* 71 (3) (2006) 235–249.
- [40] D. Varisli, T. Dogu, G. Dogu, *Chem. Eng. Sci.* 62 (2007) 5349–5352.
- [41] D. Varisli, T. Dogu, G. Dogu, *Chem. Eng. Sci.* 65 (2010) 153–159.
- [42] Y. Han, C. Lu, D. Xu, Y. Zhang, Y. Hu, He. Huang, *Appl. Catal. A* 396 (2011) 8–13.